PHYSICS

Photocarrier generation from interlayer charge-transfer transitions in WS_2-graphene heterostructures

Long Yuan,[1]* Ting-Fung Chung,[2,3]* Agnieszka Kuc,[4,5]* Yan Wan,[1] Yang Xu,[2,3] Yong P. Chen,[2,3,6] Thomas Heine,[4,5] Libai Huang[1]†

Efficient interfacial carrier generation in van der Waals heterostructures is critical for their electronic and optoelectronic applications. We demonstrate broadband photocarrier generation in WS_2-graphene heterostructures by imaging interlayer coupling–dependent charge generation using ultrafast transient absorption microscopy. Interlayer charge-transfer (CT) transitions and hot carrier injection from graphene allow carrier generation by excitation as low as 0.8 eV below the WS_2 bandgap. The experimentally determined interlayer CT transition energies are consistent with those predicted from the first-principles band structure calculation. CT interactions also lead to additional carrier generation in the visible spectral range in the heterostructures compared to that in the single-layer WS_2 alone. The lifetime of the charge-separated states is measured to be ~1 ps. These results suggest that interlayer interactions make graphene–two-dimensional semiconductor heterostructures very attractive for photovoltaic and photodetector applications because of the combined benefits of high carrier mobility and enhanced broadband photocarrier generation.

INTRODUCTION

Nanostructured materials hold great promise as building blocks to create new architectures for electronic and optoelectronic devices. Atomically thin van der Waals layers (*1*) represent a new two-dimensional (2D) material class with unusual optical and electronic properties emerging at the single- or few-layer limit (*2*–*7*), which provide opportunities to design new functionalities. Specifically, heterostructures can be formed by artificially stacking layers of different 2D materials, because traditional restrictions in heterostructure growth such as lattice-matching conditions and atom interdiffusion are no longer required (*8*–*11*). In the past few years, heterostructures constructed from graphene, hexagonal boron nitride, and semiconducting transition metal dichalcogenides (TMDCs) have established a remarkable platform for photoactive applications, including photodetectors, light-emitting diodes, and atomically thin photovoltaics (*9*, *12*–*20*).

Efficient photocarrier generation at the interfaces remains a central challenge for many of the abovementioned applications of 2D heterostructures. The structural tunability of 2D nanostructures along with atomically thin and sharp 2D interfaces provides new opportunities for controlling charge-transfer (CT) interactions at the interfaces (*21*, *22*). Charge transfer at 2D interfaces has been demonstrated to be very rapid, occurring on time scales ranging from 50 fs to a few picoseconds (*23*–*29*), and interlayer CT exciton transitions have been observed (*30*, *31*). Graphene is a versatile component to couple to TMDCs because of its high carrier mobility in combination with chemical inertness, high thermal conductance, and extraordinary stability. Heterostructures constructed from graphene and TMDCs also provide opportunities to achieve broadband charge separation below the semiconductor bandgap by using hot carrier injection from graphene (*32*). These heterostructures maintain the high mobility of graphene, which suggests that efficient extraction of carriers can be achieved at the interfaces (*20*, *33*, *34*).

A largely unexplored question is how interlayer CT interactions contribute to interfacial charge generation and separation in 2D heterostructures. Charge separation could take place directly by exciting CT transitions at the interface. Because the interlayer distance between the graphene layer and the 2D semiconductor layer could be as small as 3 Å, interlayer interactions beyond London dispersion are apparent, leading to modification of optical absorption and band structures (*34*–*38*). In addition, because practically every atom is on the surface, interfacial charge transfer is expected to play a much more important role in 2D heterostructures than in those formed by bulk materials. Although emission from interlayer CT excitons has been observed in 2D heterostructures (*30*, *31*), no direct excitation of these CT states has been reported partly due to relatively weak oscillator strengths (*39*). Here, we present a joint experimental and theoretical investigation to address charge generation from interlayer CT transitions in TMDC/graphene heterostructures. We use spatial ultrafast transient absorption microscopy (TAM) to directly compare charge generation at different interlayer coupling strengths to elucidate the role of CT transitions in WS_2-graphene heterostructures. These results demonstrate effective broadband carrier generation by excitations below the bandgap in TMDC/graphene heterostructures.

RESULTS AND DISCUSSION

Interlayer coupling–dependent charge transfer from WS_2 to graphene

The top and side views of heterostructures formed by a WS_2 layer and a graphene layer are schematically depicted in Fig. 1A. The optical micrograph of a heterostructure constructed from an exfoliated bilayer WS_2 (2L-WS_2) flake and a chemical vapor deposition (CVD)–grown graphene (G) layer on a Si/SiO_2 substrate is shown in Fig. 1B. From the atomic force microscopy (AFM) image (Fig. 1C), significant spatial heterogeneity in the contact between the 2L-WS_2 layer and the graphene layer can be observed, which is common for heterostructures fabricated by transfer methods. Specifically, there is an area with very flat morphology (area 1), whereas another area has many ripples (area 2), which indicates good contact between the graphene layer and the WS_2

[1]Department of Chemistry, Purdue University, West Lafayette, IN 47907, USA. [2]Department of Physics and Astronomy, Purdue University, West Lafayette, IN 47907, USA. [3]Birck Nanotechnology Center, Purdue University, West Lafayette, IN 47907, USA. [4]Wilhelm-Ostwald-Institut für Physikalische und Theoretische Chemie, Universität Leipzig, 04103 Leipzig, Germany. [5]Department of Physics & Earth Science, Jacobs University Bremen, 28759 Bremen, Germany. [6]School of Electrical and Computer Engineering, Purdue University, West Lafayette, IN 47907, USA.
*These authors contributed equally to this work.
†Corresponding author. Email: libai-huang@purdue.edu

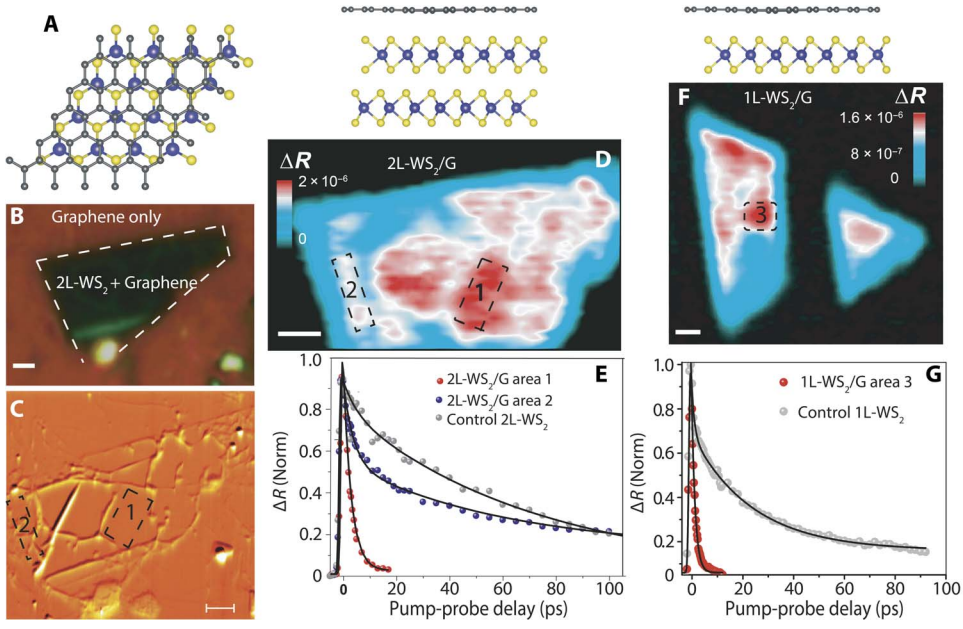

Fig. 1. Interlayer coupling–dependent charge transfer from WS_2 to graphene. (**A**) Atomic models of 1L-WS_2/G and 2L-WS_2/G interfaces, with aligned layers. (**B**) Optical image of the 2L-WS_2/G heterostructure. (**C**) AFM height image of the 2L-WS_2/G heterostructure. (**D**) Correlated TAM image of the 2L-WS_2/G heterostructure measured at 0 ps probing the A-exciton resonance. Pump photon energy, 3.14 eV; probe photon energy, 1.99 eV; pump fluence, ~2 μJ cm^{-2}. (**E**) Normalized transient dynamics of the heterostructure at areas 1 and 2 as marked, and a control 2L-WS_2 layer. Solid lines are the fitting curves with exponential decays convoluted with the experimental response function. (**F**) Correlated TAM image of the 1L-WS_2/G heterostructure measured at 0 ps probing the A-exciton resonance. Pump photon energy, 3.14 eV; probe photon energy, 1.99 eV; pump fluence, ~2 μJ cm^{-2}. (**G**) Normalized transient dynamics of the 1L-WS_2/G heterostructure at area 3 as marked, and a control 1L-WS_2 layer. Solid lines are the fitting curves with exponential decays convoluted with the experimental response function. Scale bars, 1 μm.

layer in area 1 and poor contact in area 2. The difference in contact can also be seen by the AFM line scans from areas 1 and 2, as shown in fig. S1.

The inherent spatial heterogeneity as imaged in Fig. 1C presents a major difficulty in elucidating interfacial CT dynamics in relation to interlayer coupling (*40*). To circumvent this difficulty, we use TAM with high spatial and temporal resolutions to image how interlayer coupling affects the dynamics of charge transfer from WS_2 to graphene. We first excite WS_2 at 3.14 eV and probe the A-exciton bleach at 1.99 eV to investigate charge transfer from WS_2 to graphene. A pump fluence of ~2 μJ cm^{-2} corresponds to an exciton density of ~3.6×10^{11} cm^{-2} in 1L-WS_2 (~7.2×10^{11} cm^{-2} in 2L-WS_2). To construct an image, pump-induced change in probe reflection ΔR is plotted as a function of the sample position. The spatial resolution of TAM is ~400 nm, as detailed in figs. S2 and S3. Note that the graphene-only regions of the samples have no detectable signal under the experimental conditions because of a lower absorption coefficient compared to WS_2.

The TAM image at 0 ps for the 2L-WS_2/G heterostructure is shown in Fig. 1D. As expected, better interlayer contact leads to faster charge transfer from WS_2 to graphene. The exciton decay at the strong-coupling area 1 can be fitted with a single exponential function with a decay constant of 3.0 ± 0.1 ps (Fig. 1E), similar to what has been reported previously (*24*). On the other hand, the weak-coupling area 2 shows a much slower biexponential exciton decay, with a fast component of 3.8 ± 0.3 ps (55%) and a slow component of 71.3 ± 3.0 ps (45%) (Fig. 1E). The slow decay component observed for area 2 is very similar to that from a control 2L-WS_2 flake, consistent with poor contact hampering charge transfer from WS_2 to graphene. The control 2L-WS_2 is also imaged as shown in fig. S4A, and no spatial heterogeneity is observed in exciton dynamics.

The TAM image for the 1L-WS_2/G heterostructure is shown in Fig. 1F. Similar spatial heterogeneity in dynamics is also observed in the 1L-WS_2/G heterostructure. Charge transfer at a strong-coupling location of the 1L-WS_2/G heterostructure has a characteristic time of 1.4 ± 0.1 ps (Fig. 1G), demonstrating an even stronger coupling between graphene and the 1L-WS_2 layer than in the 2L-WS_2/G heterostructure. The CT time from 1L-WS_2 to graphene is consistent with previous reports (*24*, *29*).

Carrier generation by excitation below WS_2 bandgap

We perform measurements with pump photon energies below the WS_2 bandgap, where only the interlayer CT transitions and graphene can be excited. Figure 2A plots the TA signal intensity at 0 ps probed at the A-exciton resonance (1.99 eV) in the 1L-WS_2/G heterostructure and a control 1L-WS_2 when varying the pump photon energy from 1.2 to 1.8 eV (bandgap of WS_2 is ~2 eV) with a pulse spectral width of ~20 meV. No detectable TA signal above the noise level is observed for the control 1L-WS_2 layer with pump energy lower than 1.8 eV. In contrast, both heterostructures show TA spectra that track the WS_2 A-exciton resonance with pump energy of 1.57 eV (Fig. 2B). The TA signal intensity is strongly dependent on the interlayer coupling. Figure 2C illustrates TAM images at a 0-ps time delay with 1.57-eV pump photon energy for the same 2L-WS_2/G heterostructure as shown in Fig. 1D. The TA signal intensity is higher at the strong-coupling area 1 than at the weak-coupling area 2. The overall patterns observed by TAM imaging with the 1.57-eV pump photon energy (Fig. 2C) are similar to those with the 3.14-eV pump photon energy as shown in Fig. 1D. ΔR scales linearly as a function of pump fluence, implying that the observed TA signals are due to linear absorption rather than to nonlinear two-photon excitation (Fig. 2D).

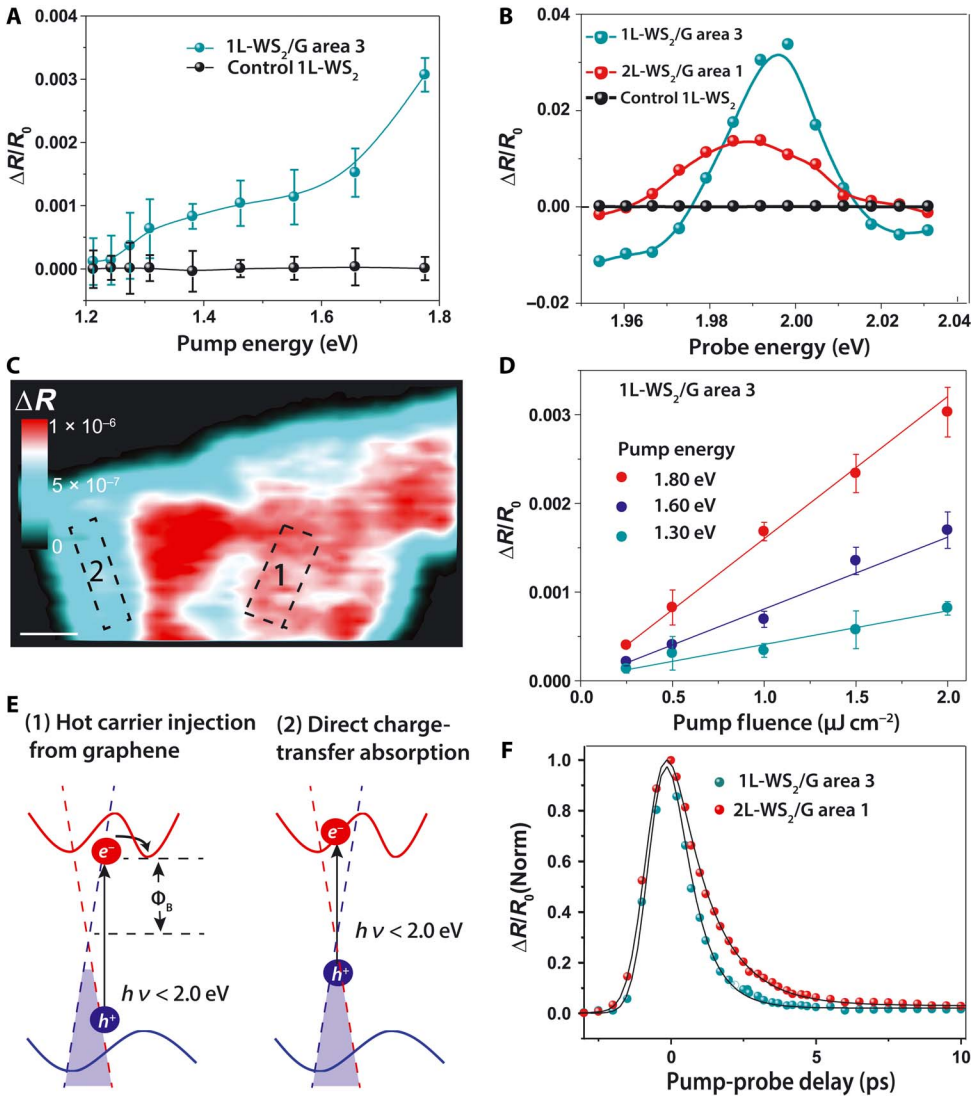

Fig. 2. Carrier generation by excitations below the WS_2 bandgap. (**A**) TA signal at 0 ps probed at 1.99 eV (A-exciton resonance) for the 1L-WS_2/G heterostructure when varying the pump photon energy from 1.2 to 1.8 eV (pump fluence, ~2 μJ cm^{-2}). (**B**) TA spectrum of the A-exciton resonance in the 1L-WS_2/G and 2L-WS_2/G heterostructures, and the control 1L-WS_2 at a 0-ps time delay with pump photon energy of 1.57 eV and pump fluence of ~17 μJ cm^{-2}. (**C**) TAM image of the 2L-WS_2/G heterostructure at 0 ps (pump, 1.57 eV; probe, 1.99 eV; pump fluence, ~17 μJ cm^{-2}). Scale bar, 1 μm. (**D**) Amplitude of the TA signal at a 0-ps time delay versus pump fluence for the 1L-WS_2/G heterostructure at area 3 showing a linear dependence at three different pump photon energies (probe, 1.99 eV). (**E**) Schematic showing two possible mechanisms. One possibility is that the graphene layer is excited and hot carrier is subsequently transferred from graphene to WS_2 (mechanism 1), and the other possibility is the direct excitation of interlayer CT transitions (mechanism 2). (**F**) Normalized transient dynamics of the 1L-WS_2/G heterostructure at area 3 and the 2L-WS_2/G heterostructure at area 1. Pump photon energy is 1.57 eV and probe photon energy is 1.99 eV. Solid lines are fits with a single exponential decay function convoluted with the experimental response function.

There are two possible mechanisms (illustrated in Fig. 2E) that could lead to the bleaching of A exciton by excitation below the WS_2 bandgap. One possibility is that the photon is absorbed by the graphene layer and hot carriers are subsequently transferred from graphene to WS_2 (mechanism 1, only electron pathway is shown) (*32*). Similar mechanism has led to the generation of photocurrent with excitations below the bandgap in graphene/WSe_2 heterostructures, as reported by Massicotte *et al.* (*32*). The absorption by graphene is due to interband transitions, creating photoexcited electrons and holes with energy $E = \frac{E_{photon}}{2}$, with respect to the Dirac point of graphene (E_{photon} is the incident photon energy). Carrier-carrier scattering establishes a quasi-equilibrium distribution in ~30 fs with an elevated effective electron temperature T_e (*41*). For hot electron injection, the Schottky barrier is equal to $\Phi_B = (E_{CBM} - E_D)$, where E_D is the Dirac point of the graphene layer and E_{CBM} is the conduction band minimum (CBM) of WS_2 (*42*, *43*). Φ_B can vary depending on the doping level of the two layers and the substrate. The hot electrons with energy larger than the barrier height Φ_B can be injected into the WS_2 layer. The number of electrons with sufficient energy is given by the Boltzmann distribution and scales with $e^{-\frac{\Phi_B}{k_B T_e}}$, where k_B is the Boltzmann constant (*32*). Similar process also exists for the holes. The other possible mechanism is through direct excitation of interlayer CT transitions (mechanism 2 in Fig. 2E), where electrons can be promoted from graphene to WS_2 (shown in Fig. 2E) or holes promoted from WS_2 to graphene (not shown). For mechanism 2, the momentum

of graphene and WS_2 needs to be taken into account and the transition energies will be discussed in the following section.

Both hot carrier injection and direct CT absorption mechanisms can lead to a charge-separated state, where the electron (hole) resides in the WS_2 and the hole (electron) remains on the graphene layer. Consequently, the bleaching of A-exciton transition results from Pauli blocking and/or bandgap renormalization in WS_2 (*44*). The dynamics of charge generation and recombination has been measured following the 1.57-eV pump excitation (Fig. 2F). For mechanism 1, a risetime is expected corresponding to hot carrier transfer from graphene. In contrast, direct excitation of the CT transitions should lead to an instantaneous rise of the TA signal. The TA signal rise is instantaneous within a pulse width of ~300 fs for both the 1L-WS_2/G and 2L-WS_2/G heterostructures (Fig. 2F), probably due to the fact that the time resolution of our experiments is not sufficient to resolve hot carrier injection from graphene. In the1L-WS_2/G heterostructure, the recombination of the electrons and holes at the interface is 0.78 ± 0.04 ps, which is shorter than that of 1.30 ± 0.03 ps in the 2L-WS_2/G heterostructure. The faster recombination in the 1L-WS_2/G heterostructure suggests that the interfacial charge-separated states are dependent on the detailed electronic coupling at interfaces (*21*). The interfacial electron-hole interaction strength decreases as the thickness of TMDC increases, because the additional layers screen the interaction (*45*, *46*). For the charge-separated states, the spatial indirect nature (that is, electrons and holes reside in different layers) should dictate the recombination process. The indirect intralayer exciton band structure of 2L-WS_2 probably does not play an important role in determining the lifetime of interfacial charge recombination.

Both mechanisms illustrated in Fig. 2E could contribute to the TA signal; however, it is highly challenging to separate these two contributions. In principle, although linear absorption could directly measure the CT transitions from mechanism 2, this is a difficult task because of the weak oscillator strengths (*47*). For instance, the interlayer exciton oscillator strength in $MoSe_2$/WSe_2 heterostructures is at least 20 times weaker than that of the intralayer exciton (*39*). To separate the contribution from the two mechanisms, we examined the pump fluence dependence when excited below the WS_2 bandgap. As demonstrated by Massicotte *et al.* (*32*), the photocurrent exhibits a P^{α} ($\alpha > 1$) dependence on the pump fluence due to the hot carrier injection contribution when excited below the bandgap of WSe_2, which can be explained by the fact that the number of electrons with sufficient energy scales with $e^{-\frac{\Phi_B}{k_B T_e}}$. In contrast, direct absorption by WSe_2 above the bandgap leads to a linear power dependence ($\alpha = 1$) (*32*). As shown in Fig. 2D, a linear dependence (that is, $\Delta R \propto P$, $\alpha = 1$) is observed for excitations at 1.30, 1.60, and 1.80 eV in the 1L-WS_2/G heterostructure, which could not be explained by hot carrier injection from graphene. A linear pump fluence dependence is also observed for the 2L-WS_2/G heterostructure when excited at 1.57 eV (fig. S5). On the other hand, direct CT absorption (mechanism 2) should lead to the linear power dependence similar to the absorption by WS_2 above the bandgap. Therefore, we conclude that direct CT absorption also contributes to the observed TA signal in the 1L-WS_2/G and 2L-WS_2/G heterostructures when excited below the WS_2 bandgap. We note that the WSe_2 in the graphene/WSe_2 heterostructures studied by Massicotte *et al.* (*32*) are multilayer (3 to more than 100 layers), and the contribution from interlayer CT absorption to the photocurrent should be much weaker than in the heterostructures based on the 1L-WS_2 investigated here. This is because the oscillator strength of the CT transitions decreases as the thickness of the TMDC increases, as the additional layers screen the electron-hole interaction in the CT states (*45*, *46*). The decreased exciton oscillator strength as the dielectric constant increases has been observed in single-walled carbon nanotubes (*45*).

First-principles calculation of interlayer CT transitions

To identify possible interlayer CT transitions, we performed band structure calculation for the 1L-WS_2/G heterostructure from first principles using density functional theory (DFT). We considered two models, the commensurate and incommensurate. In the first model, we take a 4×4 WS_2 and a 5×5 graphene supercell, because the lattice vectors of these two cells have a mismatch of only 2.3%. We then average both lattice vectors so that 4×4 WS_2 and 5×5 graphene supercell sizes match exactly. This results in small stretching of the WS_2 monolayer and compression of the graphene layer. The corresponding band structure (Fig. 3A) is an almost perfect superposition of the two individual band structures of graphene and WS_2, that is, the band edges of both systems are kept almost unaffected by one another, and we can determine the band shift of the WS_2 with respect to graphene: Conduction band of WS_2 is situated at about 1 eV above the Dirac point of graphene. Note that the Dirac point might not be the most precise in the present context, because there is a small band gap (~11 meV) opening in the heterostructure.

Because the lattices in the actual heterostructures are not aligned, we next consider an incommensurate model to account for a large lattice mismatch of ~22% (lattice constant of graphene is 2.46 Å and that of WS_2 is 3.15 Å). Although this first-principles calculation is not computationally feasible at present, we calculated the separate perfect monolayers and plotted their band structure as an overlap, with the shift of the band edges calculated in the previous step. The result for the Γ-K direction is shown in Fig. 3B. Because of the lattice mismatch, the Brillouin zones are also shifted with respect to each other. Therefore, the K points do not overlap in every cell, in contrast to the commensurate model. As shown in Fig. 3B, additional interlayer excitations exist in the incommensurate lattices, which allow the excited electrons from graphene to WS_2 or holes from WS_2 to graphene that could enhance carrier generation. However, the interlayer excitations are not observed for the other direction along the Γ-M path (see fig. S6).

The interlayer CT transitions below the bandgap of WS_2 are identified in Fig. 3B. There is a transition of electron from the K point of graphene to the K point of WS_2 at 1.04 eV, a transition from the K point of graphene to the conduction band of WS_2 near the Γ point with an energy of 1.22 eV, and a transition at 1.54 eV from the K point of graphene to between the Γ and K point of WS_2. Note that inherent errors of DFT neglect exciton binding energy and may introduce a constant energy shift of the conduction band. According to high-level calculations on a single-layer WS_2, the error in predicting the transition energies should be no more than 0.5 eV (*48*). In addition, the graphene layer is p-doped with a Fermi level shifted by ~0.17 eV, as determined by Raman spectroscopy (fig. S7). Taking these two effects into account, the predicted transition energies are consistent with the absorption band of 1.2 to 1.8 eV, as shown in Fig. 2A. On the basis of the agreement, we assign the interlayer transitions observed to electrons from the valence bands of graphene that are promoted to the conduction bands of WS_2. We cannot entirely rule out the transitions prompting holes from WS_2 to graphene, and they probably also contribute. Note that our model in Fig. 3B is incomplete, and it reflects only one WS_2/graphene rotation angle (with matching lattice orientations). Therefore, the intensities of the interlayer excitations may be dependent on the mutual rotation of

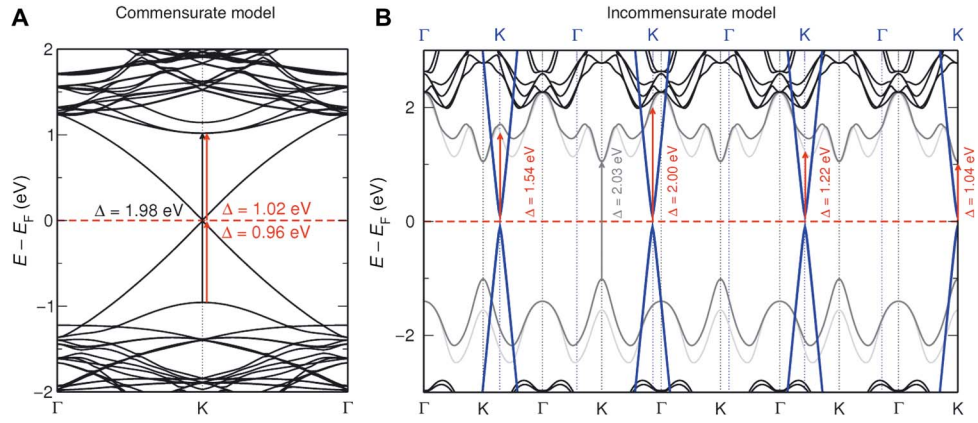

Fig. 3. Band structure of the heterostructure. (**A**) Commensurate model of a 5 × 5 graphene/4 × 4 WS_2 supercell (at the PBE level) and (**B**) incommensurate model of corresponding perfect unit cells (as in a single layer) of each component (at the HSE06/SOC level) along the Γ-K direction. The red arrows indicate interlayer transitions.

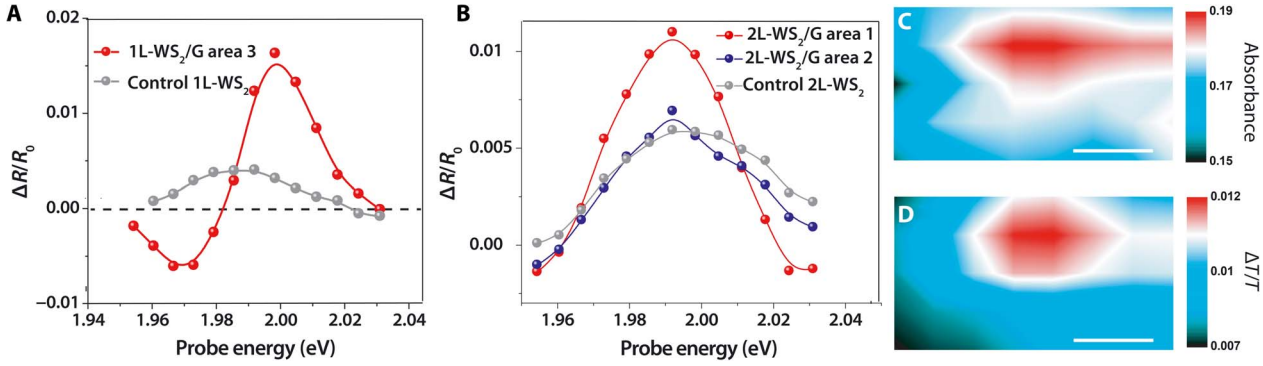

Fig. 4. Enhanced carrier generation by excitation above the WS_2 bandgap at 3.14 eV. (**A**) TA spectrum of the A-exciton resonance of the same 1L-WS_2/G heterostructure shown in Fig. 1F along with a control 1L-WS_2 layer at a 0-ps time delay and pump fluence of ~2 μJ cm^{-2}. (**B**) TA spectrum of the A-exciton resonance (time delay, 0 ps; pump fluence, ~2 μJ cm^{-2}) at different positions of the same 2L-WS_2/G heterostructure shown in Fig. 1D and for the control 2L-WS_2 layer. Zoomed-in linear absorption (**C**) and correlated TAM image (**D**) of the 1L-WS_2/G heterostructure on a transparent sapphire substrate. The TAM image is measured at 0 ps (pump, 3.14 eV; probe, 1.99 eV). Scale bars, 200 nm.

the layers. However, the CT transition energies should still fall within the same range of 1 to 2 eV regardless of the rotation angle, because the band structure of the heterostructure is almost perfectly the superposition of that of graphene and WS_2. Further, because of a large lattice mismatch of ~22% and the polycrystalline nature of the CVD graphene, many rotation angles likely coexist in the heterostructures measured experimentally. Therefore, the measured CT transition energies are probably the average of many rotation angles. The interlayer CT transition energies can be potentially modulated by tuning the Fermi level of graphene, which will be addressed in future studies.

Enhanced carrier generation by excitation above the bandgap

With excitation above the WS_2 bandgap at 3.14 eV, TA signal intensities at 0 ps for the strong-coupling areas are higher than those for the weak-coupling areas. The TA intensity for the 1L-WS_2/G heterostructure is enhanced by a factor of 4 over the control, as shown in Fig. 4A. The TA intensity at the strong-coupling area 1 in the 2L-WS_2/G heterostructure is about two times higher than the control, whereas the weak-coupling area 2 has a TA amplitude similar to that of the control (Fig. 4B). A higher TA intensity correlated with stronger interlayer coupling implies that the nature of the photoexcited state in WS_2 is dependent on the interlayer coupling strength. A control 2L-WS_2 is also imaged as shown in fig. S4, and no spatial heterogeneity is observed in the TA signal intensity (the SDs of ΔR at 0 and 5 ps are 3.4% and 3.8%, respectively). Raman intensity from the heterostructures is also enhanced over the control (fig. S8). We note here that the enhanced TA signal in the WS_2/G heterostructure has been observed previously (*24*); however, no explanation has been given.

Because the TA signal results from combined Pauli blocking and bandgap renormalization effects (*44*, *49*), there are two possible reasons for the increased TA intensities at strong-coupling locations: (i) The absorption above the bandgap is increased by the interlayer CT transitions and an increased TA intensity is due to Pauli blocking and (ii) photoexcitation of CT transitions leads to larger bandgap renormalization effects than excitons. Note that transient bandgap renormalization observed here is due to further modifications of the exciton energy upon photoexcitation beyond the static effect (*49*, *50*). To directly measure the interlayer coupling–dependent absorption at 3.14 eV, we imaged correlated reflection and transmission of 1L-WS_2/G on a transparent sapphire substrate (fig. S9). The linear absorption is deduced using approaches described in Materials and Methods. The linear absorption and correlated TAM image are shown in Fig. 4 (C and D). Both linear absorption and transient absorption are increased at a strong-coupling location. Having graphene on top leads to static bandgap renormalization of WS_2 and reduces the exciton binding energy (*51*, *52*). It is possible that

the increased linear absorption is due to static screening from graphene that modifies the absorption of WS_2 instead of the absorption by the CT transitions. However, the absorption at 3.14 eV is not near any exciton resonances, and therefore, the change in the absorption due to static screening from graphene should not be significant. Although linear absorption increased by ~25% at a strong-coupling location compared to a weak-coupling location (Fig. 4C), the TA signal intensity at the same location is increased by ~70% (Fig. 4D), indicating that the increased absorption accounts partially for the increased TA intensity. The linear absorption and the TA images do not look exactly the same, probably due to the higher spatial resolution of TAM being a two-photon technique (*53*) or interlayer (WS_2 and graphene) orientation.

An additional TA signal increase at strong-coupling locations is likely due to a larger transient bandgap renormalization effect induced by the photoexcited CT states. The TA spectrum at the strong-coupling location in 1L-WS_2/G has a derivative shape with a new red-shifted photoinduced absorption band, in contrast to the control 1L-WS_2 (Fig. 4A). The derivative-shaped TA spectrum is a signature of transient bandgap renormalization because of the screening of excitons by photogenerated carriers or excitons (*44*). The transient reduction of the optical bandgap is estimated by taking the energy difference between the positive peak and the negative peak to be ~30 meV for the 1L-WS_2/G heterostructure, as shown in Fig. 4A. Similar transient bandgap renormalization has also been observed for another 1L-WS_2/G heterostructure on a sapphire substrate (fig. S10). To verify that the transient bandgap renormalization effects observed are not just due to a higher exciton density, we measured the TA spectrum of 1L-WS_2 at an exciton density from 7.2×10^{11} cm^{-2} to 2.9×10^{12} cm^{-2} (see fig. S11). Even at a higher exciton density (eight times) than that in the measurements of Fig. 4A, no obvious transient bandgap renormalization has been observed. We note that Sie *et al.* (*50*) reported the exciton red shift at an exciton density of as low as 10^{11} cm^{-2} under a similar nonresonant excitation condition, which is somewhat inconsistent with our results.

The larger transient bandgap renormalization effects at the strong-coupling locations could be explained by the lower binding energy of the interfacial CT states than that for the A excitons in WS_2 (~200 meV when it is covered by graphene) (*52*). Because of the spatially separated nature and the efficient screening of Coulomb interaction by graphene, electrons and holes generated at the interface from the CT states are more "free" and can potentially screen the Coulomb interaction more effectively than the A excitons, which result in a larger shift in the exciton resonance. Examination of the photoluminescence spectra reveals that the relative intensity of the trion emission to that of the neutral exciton is higher in the 1L-WS_2/G heterostructure than in the control WS_2 (fig. S12), consistent with the higher density of free carriers.

Potential to extract carriers generated by the CT states

The lifetime of the charge-separated states at the graphene-WS_2 interface has been measured to be ~1 ps (Fig. 2F). Although the charge-separated states live relatively short, the high carrier mobility of graphene on WS_2 makes it very promising to harvest these charge carriers. For instance, an electron mobility of 38,000 $cm^2 V^{-1} s^{-1}$ at room temperature has been measured for graphene on the WS_2 substrate (*33*), similar to that of graphene on hexagonal boron nitride. Ultrafast carrier extraction from graphene in as short as 50 fs has been demonstrated (*54*); therefore, the 1-ps lifetime should be sufficiently long. Although our measurements do not directly measure the electron-hole binding energy at the interface, successful charge extraction has been confirmed in graphene/WS_2 photodetector devices (*13*, *32*), which is probably facilitated by a built-in field at the interface. Therefore, the binding energy of these interlayer states can be overcome to achieve extraction.

CONCLUSION

In summary, ultrafast microscopy in combination with first-principles calculation provides a comprehensive picture of carrier generation resulting from interlayer coupling in WS_2-graphene heterostructures. Interlayer CT transitions and hot carrier injection promote electrons from graphene to WS_2, allowing carrier generation by excitation of CT transitions below the WS_2 bandgap and leading to enhancement in photocarrier generation by visible optical excitation. The CT transition energies predicted by first-principles calculations have been verified by experimental measurements. Broadband enhancement in carrier generation is highly attractive for photovoltaic applications of heterostructures based on graphene and 2D semiconductors.

MATERIALS AND METHODS

Heterostructure fabrication

1L- and 2L-WS_2 were mechanically exfoliated from bulk WS_2 crystals (2D Semiconductors Inc.) onto the Si wafer with a 90-nm-thick oxide. The number of layers was confirmed by using a combination of photoluminescence and Raman spectroscopy (*55*). Monolayer graphene film was grown on copper (Cu) foils at atmospheric pressure using CVD (*56*). The CVD-grown graphene used in this work was polycrystalline with an average grain size of ~15 μm. The heterostructures were assembled by depositing CVD-grown graphene on top of 1L- and 2L-WS_2 using an alternative poly(methyl methacrylate) (PMMA) transfer process to minimize aqueous solution at the graphene-WS_2 interface (*57*, *58*). The CVD-grown graphene on Cu foil was spin-coated (3000 rpm) with 950PMMA-A4 (MicroChem). PMMA-coated graphene was adhered to a polymer frame with a hole at the center and suspended by Cu etching. Residual etchant was diluted with deionized water. The PMMA/graphene membrane was gently blown dry with nitrogen and then brought into contact with WS_2 layers followed by baking at around 350 K for 5 min to promote adhesion between graphene and WS_2. Finally, the heterostructure was annealed at 420 K in vacuum of 10^{-5} torr for 2 hours followed by natural cooling. The orientation of WS_2 and graphene layers is not aligned in any particular way in the momentum space.

Transient absorption microscopy and spectroscopy

Transient absorption measurements were taken using a homebuilt TAM system performed in reflection mode, as shown schematically in fig. S2. Briefly, a Ti:sapphire oscillator (Coherent Mira 900) pumped by a Verdi diode laser (Verdi V18) was used as the light source (output at 790 nm, repetition rate of 80 MHz). Seventy percent of the pulse energy was fed into the optical parametric oscillator (Coherent Mira OPO) to generate probe light between 610 and 640 nm, whereas the remaining 30% was doubled to 395 nm using a β-barium borate crystal. The pump beam was modulated at 1 MHz using an acoustic optical modulator (model R21080-1DM, Gooch & Housego). A 40× objective [numerical aperture (NA) = 0.60] was used to focus both pump and probe beams onto the sample, and the reflection light was then collected by the same objective and detected by an avalanche Si photodiode (Hamamatsu). The change in the probe reflection (ΔR) induced by the pump was detected by a lock-in amplifier (HF2LI, Zurich Instrument). For transient dynamics scans, pump and probe beams were overlapped

spatially and a mechanical translation stage (Thorlabs, LTS300) was used to delay the probe with respect to the pump. For morphological TAM imaging, pump and probe beams were overlapped spatially and a piezoelectric stage (P-527.3Cl, Physik Instrumente) with a step size of 100 nm was used to scan the sample. For the reflectance contrast measurements, the pump beam was blocked and only the reflection signal of the probe beam was detected. Transient absorption spectrum is defined as $\Delta R/R_0$, where ΔR and R_0 are the change in the probe reflection induced by the pump and the probe reflection from the area without the sample, respectively.

For the measurement with tunable pump photon energy (Fig. 2A), the output of a high–repetition rate amplifier (Pharos Light Conversion, 400 kHz, 1030 nm) pumped two independent optical parametric amplifiers (OPAs), one providing the pump (between 1.2 and 1.8 eV) and the other supplying the probe (1.99 eV). Both the pump and probe beams were spatially filtered. An acousto-optic modulator (Gooch & Housego, R23080-1) was used to modulate the pump beam at 100 kHz. The change in the probe reflection (ΔR) induced by the pump was detected by a lock-in amplifier (Stanford Research Instrument). All optical measurements were performed under ambient conditions.

Linear absorption microscopy

We doubled the fundamental light (1.57 eV) from a Ti:sapphire oscillator (Coherent Mira 900) to measure the linear absorption at 3.14 eV of CVD-WS_2/G on a transparent sapphire substrate. A 40× objective (NA = 0.60) was used to focus light onto the sample. Both the transmission and reflection light were then collected and detected by avalanche Si photodiodes (Hamamatsu). The absorption of WS_2/G was calculated by using the graphene-only region on the same substrate as the reference and solving the following two equations together

$$I = T_g + CR_g + A_g \times I \text{(on the reference graphene-only region)}$$
$$I = T_{WS_2/G} + CR_{WS_2/G} + A_{WS_2/G} \times I \text{(on the heterostructure region)}$$

where I is the total incident light intensity, T_g is the transmitted light intensity of graphene, R_g is the reflection light intensity of graphene, A_g is the absorption of graphene, $T_{WS_2/G}$ is the transmitted light intensity of WS_2/G, $R_{WS_2/G}$ is the reflection light intensity of WS_2/G, $A_{WS_2/G}$ is the absorption of WS_2/G, and C is the collection efficiency of the reflection arm. We used an A_g value of 0.0424 for graphene at 3.14 eV from a previous report (*59*).

Atomic force microscopy

The surface morphology of the heterostructure was inspected using an NT-MDT NTEGRA Prima multifunctional AFM in the tapping mode.

First-principles calculations

All systems were fully optimized (atomic positions and lattice vectors) within DFT. In the commensurate model, we averaged the lattice vectors of graphene and WS_2 using 5 × 5 and 4 × 4 unit cells, respectively. This results in the lattice parameter a = 12.433 Å, corresponding to 0.6% stretch of graphene and 1.7% compression of WS_2. In the incommensurate model, we superposed the band structure of perfect monolayers of graphene and WS_2 for the presentation of the band structure and the mismatch of the Brillouin zones of both materials. The models were fully optimized using CRYSTAL09 (*60*) with the following basis sets: C 6-21G* (*61*), S 86-311G* (*62*), W large-core effective core potential (ECP) (*63*), and the Perdew-Burke-Ernzerhof (PBE) functional (*64*) with the D3 dispersion correction proposed by Grimme (*65*). Band structures were obtained from the Vienna Ab initio Simulation Package (VASP) code (*66*–*68*) using projector-augmented waves with energy cutoffs of 500 eV for the commensurate model and 600 eV for the unit cells. We used the HSE06 functional (*69*) together with the spin-orbit coupling for the incommensurate band structure representation, whereas the commensurate system was treated using PBE. The layered models were calculated with a 20 Å vacuum to ensure negligible interactions with the neighboring cells in the 3D periodic boundary condition representation. The dispersion corrections were treated at the D3 level. K-point meshes of 3 × 3 × 1 and 6 × 6 × 1 were used for the larger and smaller models, respectively.

SUPPLEMENTARY MATERIALS

Supplementary material for this article is available at http://advances.sciencemag.org/cgi/content/full/4/2/e1700324/DC1

section S1. Spatial resolution and sensitivity of TAM
section S2. Raman spectroscopy
section S3. Steady-state PL measurements of the 1L-WS_2/G heterostructure
fig. S1. AFM measurement of the 2L-WS_2/G heterostructure.
fig. S2. Schematics of homebuilt TAM setup.
fig. S3. Spatial resolution of TAM.
fig. S4. TAM images of a control 2L-WS_2.
fig. S5. The amplitude of the TA signal at a 0-ps time delay versus pump fluence for the 2L-WS_2/G heterostructure at area 1 (pump, 1.57 eV; probe, 1.99 eV).
fig. S6. Band structure calculation along the Γ-M path.
fig. S7. Raman spectra of the 1L-WS_2/G heterostructure with an excitation energy of 1.96 eV and the Fermi level shift of graphene.
fig. S8. Enhancement of Raman intensity in the WS_2/G heterostructures with an excitation energy of 2.32 eV.
fig. S9. Correlated transmission and reflection images of the same 1L-WS_2/G heterostructure on a transparent sapphire substrate shown in Fig. 4 (C and D).
fig. S10. TA spectrum of the A-exciton resonance for strong- and weak-coupling locations of the 1L-WS_2/G heterostructure on a sapphire substrate.
fig. S11. Pump intensity–dependent TA spectra of a control 1L-WS_2 flake.
fig. S12. PL spectra of the 1L-WS_2/G and a control 1L-WS_2 excited at 2.78 eV.
References (*70*–*73*)

REFERENCES AND NOTES

1. K. Novoselov, D. Jiang, F. Schedin, T. J. Booth, V. V. Khotkevich, S. V. Morozov, A. K. Geim, Two-dimensional atomic crystals. *Proc. Natl. Acad. Sci. U.S.A.* **102**, 10451–10453 (2005).
2. K. S. Novoselov, A. K. Geim, S. V. Morozov, D. Jiang, M. I. Katsnelson, I. V. Grigorieva, S. V. Dubonos, A. A. Firsov, Two-dimensional gas of massless Dirac fermions in graphene. *Nature* **438**, 197–200 (2005).
3. A. K. Geim, Graphene: Status and prospects. *Science* **324**, 1530–1534 (2009).
4. F. Bonaccorso, Z. Sun, T. Hasan, A. C. Ferrari, Graphene photonics and optoelectronics. *Nat. Photonics* **4**, 611–622 (2010).
5. A. Splendiani, L. Sun, Y. Zhang, T. Li, J. Kim, C. Y. Chim, G. Galli, F. Wang, Emerging photoluminescence in monolayer MoS_2. *Nano Lett.* **10**, 1271–1275 (2010).
6. K. F. Mak, C. Lee, J. Hone, J. Shan, T. F. Heinz, Atomically thin MoS_2: A new direct-gap semiconductor. *Phys. Rev. Lett.* **105**, 136805 (2010).
7. A. Chernikov, T. C. Berkelbach, H. M. Hill, A. Rigosi, Y. Li, O. B. Aslan, D. R. Reichman, M. S. Hybertsen, T. F. Heinz, Exciton binding energy and nonhydrogenic Rydberg series in monolayer WS_2. *Phys. Rev. Lett.* **113**, 076802 (2014).
8. K. S. Novoselov, A. H. Castro Neto, Two-dimensional crystals-based heterostructures: Materials with tailored properties. *Phys. Scr.* **T146**, 014006 (2012).
9. A. K. Geim, I. V. Grigorieva, Van der Waals heterostructures. *Nature* **499**, 419–425 (2013).
10. B. V. Lotsch, Vertical 2D heterostructures. *Annu. Rev. Mater. Res.* **45**, 85–109 (2015).
11. G. S. Duesberg, Heterojunctions in 2D semiconductors: A perfect match. *Nat. Mater.* **13**, 1075–1076 (2014).
12. M. Bernardi, M. Palummo, J. C. Grossman, Semiconducting monolayer materials as a tunable platform for excitonic solar cells. *ACS Nano* **6**, 10082–10089 (2012).
13. L. Britnell, R. M. Ribeiro, A. Eckmann, R. Jalil, B. D. Belle, A. Mishchenko, Y.-J. Kim, R. V. Gorbachev, T. Georgiou, S. V. Morozov, A. N. Grigorenko, A. K. Geim, C. Casiraghi, A. H. Castro Neto, K. S. Novoselov, Strong light-matter interactions in heterostructures of atomically thin films. *Science* **340**, 1311–1314 (2013).
14. F. Withers, O. Del Pozo-Zamudio, A. Mishchenko, A. P. Rooney, A. Gholinia, K. Watanabe, T. Taniguchi, S. J. Haigh, A. K. Geim, A. I. Tartakovskii, K. S. Novoselov, Light-emitting diodes by band-structure engineering in van der Waals heterostructures. *Nat. Mater.* **14**, 301–306 (2015).

15. W. J. Yu, Y. Liu, H Zhou, A. Yin, Z. Li, Y. Huang, X. Duan, Highly efficient gate-tunable photocurrent generation in vertical heterostructures of layered materials. *Nat. Nanotechnol.* **8**, 952–958 (2013).
16. F. H. L. Koppens, T Mueller, P. Avouris, A. C. Ferrari, M. S. Vitiello, M. Polini, Photodetectors based on graphene, other two-dimensional materials and hybrid systems. *Nat. Nanotechnol.* **9**, 780–793 (2014).
17. D. Jariwala, V. K. Sangwan, L. J. Lauhon, T. J. Marks, M. C. Hersam, Emerging device applications for semiconducting two-dimensional transition metal dichalcogenides. *ACS Nano* **8**, 1102–1120 (2014).
18. M. Y. Li, Y. Shi, C.-C. Cheng, L.-S. Lu, Y.-C. Lin, H.-L. Tang, M.-L. Tsai, C.-W. Chu, K.-H. Wei, J.-H. He, W.-H. Chang, K. Suenaga, L.-J. Li, Epitaxial growth of a monolayer WSe_2-MoS_2 lateral p-n junction with an atomically sharp interface. *Science* **349**, 524–528 (2015).
19. J. H. Yu, H. R. Lee, S. S. Hong, D. Kong, H.-W. Lee, H. Wang, F. Xiong, S. Wang, Y. Cui, Vertical heterostructure of two-dimensional MoS_2 and WSe_2 with vertically aligned layers. *Nano Lett.* **15**, 1031–1035 (2015).
20. M. Massicotte, P. Schmidt, F. Vialla, K. G. Schädler, A. Reserbat-Plantey, K. Watanabe, T. Taniguchi, K. J. Tielrooij, F. H. L. Koppens, Picosecond photoresponse in van der Waals heterostructures. *Nat. Nanotechnol.* **11**, 42–46 (2015).
21. X. Zhu, N. R. Monahan, Z. Gong, H. Zhu, K. W. Williams, C. A. Nelson, Charge transfer excitons at van der Waals interfaces. *J. Am. Chem. Soc.* **137**, 8313–8320 (2015).
22. R. Long, O. V. Prezhdo, Quantum coherence facilitates efficient charge separation at a MoS_2/$MoSe_2$ van der Waals junction. *Nano Lett.* **16**, 1996–2003 (2016).
23. X. Hong, J. Kim, S.-F. Shi, Y. Zhang, C. Jin, Y. Sun, S. Tongay, J. Wu, Y. Z., F. Wang, Ultrafast charge transfer in atomically thin MoS_2/WS_2 heterostructures. *Nat. Nanotechnol.* **9**, 682–686 (2014).
24. J. He, N. Kumar, M. Z. Bellus, H.-Y. Chiu, D. He, Y. Wang, H. Zhao, Electron transfer and coupling in graphene-tungsten disulfide van der Waals heterostructures. *Nat. Commun.* **5**, 5622 (2014).
25. A. F. Rigosi, H. M. Hill, Y. Li, A. Chernikov, T. F. Heinz, Probing interlayer interactions in transition metal dichalcogenide heterostructures by optical spectroscopy: MoS_2/WS_2 and $MoSe_2$/WSe_2. *Nano Lett.* **15**, 5033–5038 (2015).
26. Y. Yu, S. Hu, L. Su, L. Huang, Y. Liu, Z. Jin, A. A. Purezky, D. B. Geohegan, K. W. Kim, Y. Zhang, L. Cao, Equally efficient interlayer exciton relaxation and improved absorption in epitaxial and nonepitaxial MoS_2/WS_2 heterostructures. *Nano Lett.* **15**, 486–491 (2015).
27. D. Kozawa, A. Carvalho, I. Verzhbitskiy, F. Giustiniano, Y. Miyauchi, S. Mouri, A. H. Castro Neto, K. Matsuda, G. Eda, Evidence for fast interlayer energy transfer in $MoSe_2$/WS_2 heterostructures. *Nano Lett.* **16**, 4087–4093 (2016).
28. H. Zhu, J. Wang, Z. Gong, Y. D. Kim, J. Hone, X. Y. Zhu, Interfacial charge transfer circumventing momentum mismatch at two-dimensional van der Waals heterojunctions. *Nano Lett.* **17**, 3591–3598 (2017).
29. H. M. Hill, A. F. Rigosi, Archana Raja, A. Chernikov, C. Roquelet, T. F. Heinz, Exciton broadening in WS_2/graphene heterostructures. *Phys. Rev. B* **96**, 205401 (2017).
30. P. Rivera, J. R. Schaibley, A. M. Jones, J. S. Ross, S. Wu, G. Aivazian, P. Klement, K. Seyler, G. Clark, N. J. Ghimire, J. Yan, D. G. Mandrus, W. Yao, X. Xu, Observation of long-lived interlayer excitons in monolayer $MoSe_2$–WSe_2 heterostructures. *Nat. Commun.* **6**, 6242 (2015).
31. H. Heo, J. H. Sung, S. Cha, B.-G. Jang, J.-Y. Kim, G. Jin, D. Lee, J.-H. Ahn, M.-J. Lee, J. H. Shim, H. Choi, M.-H. Jo, Interlayer orientation-dependent light absorption and emission in monolayer semiconductor stacks. *Nat. Commun.* **6**, 7372 (2015).
32. M. Massicotte, P. Schmidt, F. Vialla, K. Watanabe, T. Taniguchi, K. J. Tielrooij, F. H. L. Koppens, Photo-thermionic effect in vertical graphene heterostructures. *Nat. Commun.* **7**, 12174 (2016).
33. J. Y. Tan, A. Avsar, J. Balakrishnan, G. K. W. Koon, T. Taychatanapat, E. C. T. O'Farrell, K. Watanabe, T. Taniguchi, G. Eda, A. H. Castro Neto, B. Özyilmaz, Electronic transport in graphene-based heterostructures. *Appl. Phys. Lett.* **104**, 183504 (2014).
34. M. Ghorbani-Asl, P. D. Bristowe, K. Koziol, T. Heine, A. Kuc, Effect of compression on the electronic, optical and transport properties of MoS_2/graphene-based junctions. *2D Mater.* **3**, 025018 (2016).
35. A. Du, S. Sanvito, Z. Li, D. Wang, Y. Jiao, T. Liao, Q. Sun, Y. H. Ng, Z. Zhu, R. Amal, S. C. Smith, Hybrid graphene and graphitic carbon nitride nanocomposite: Gap opening, electron–hole puddle, interfacial charge transfer, and enhanced visible light response. *J. Am. Chem. Soc.* **134**, 4393–4397 (2012).
36. K. Wang, B. Huang, M. Tian, F. Ceballos, M. W. Lin, M. Mahjouri-Samani, A. Boulesbaa, A. A. Puretzky, C. M. Rouleau, M. Yoon, H. Zhao, K. Xiao, G. Duscher, D. B. Geohegan, Interlayer coupling in twisted WSe_2/WS_2 bilayer heterostructures revealed by optical spectroscopy. *ACS Nano* **10**, 6612–6622 (2016).
37. H. C. Diaz, J. Avila, C. Chen, R. Addou, M. C. Asensio, M. Batzill, Direct observation of interlayer hybridization and Dirac relativistic carriers in graphene/MoS_2 van der Waals heterostructures. *Nano Lett.* **15**, 1135–1140 (2015).
38. W. Jin, P.-C. Yeh, N. Zaki, D. Chenet, G. Arefe, Y. Hao, A. Sala, T. Onur Mentes, J. I. Dadap, A. Locatelli, J. Hone, R. M. Osgood Jr., Tuning the electronic structure of monolayer graphene/Mo S_2 van der Waals heterostructures via interlayer twist. *Phys. Rev. B* **92**, 201409 (2015).
39. J. S. Ross, P. Rivera, J. Schaibley, E. Lee-Wong, H. Yu, T. Taniguchi, K. Watanabe, J. Yan, D. Mandrus, D. Cobden, W. Yao, X. Xu, Interlayer exciton optoelectronics in a 2D heterostructure p–n junction. *Nano Lett.* **17**, 638–643 (2017).
40. S. Tongay, W. Fan, J. Kang, J. Park, U. Koldemir, J. Suh, D. S. Narang, K. Liu, J. Ji, J. Li, R. Sinclair, J. Wu, Tuning interlayer coupling in large-area heterostructures with CVD-grown MoS_2 and WS_2 monolayers. *Nano Lett.* **14**, 3185–3190 (2014).
41. M. Breusing, C. Ropers, T. Elsaesser, Ultrafast carrier dynamics in graphite. *Phys. Rev. Lett.* **102**, 086809 (2009).
42. Y. Liu, P. Stradins, S.-H. Wei, Van der Waals metal-semiconductor junction: Weak Fermi level pinning enables effective tuning of Schottky barrier. *Sci. Adv.* **2**, e1600069 (2016).
43. S. Forti, A. Rossi, H. Büch, T. Cavallucci, F. Bisio, A. Sala, T. O. Menteş, A. Locatelli, M. Magnozzi, M. Canepa, K. Müller, S. Link, U. Starke, V. Tozzini, C. Coletti, Electronic properties of single-layer tungsten disulfide on epitaxial graphene on silicon carbide. *Nanoscale* **9**, 16412–16419 (2017).
44. E. A. A. Pogna, M. Marsili, D. De Fazio, S. Dal Conte, C. Manzoni, D. Sangalli, D. Yoon, A. Lombardo, A. C. Ferrari, A. Marini, G. Cerullo, D. Prezzi, Photo-induced bandgap renormalization governs the ultrafast response of single-layer MoS_2. *ACS Nano* **10**, 1182–1188 (2016).
45. V. Perebeinos, J. Tersoff, P. Avouris, Scaling of excitons in carbon nanotubes. *Phys. Rev. Lett.* **92**, 257402 (2004).
46. A. Raja, A. Montoya-Castillo, J. Zultak, X. X. Zhang, Z. Ye, C. Roquelet, D. A. Chenet, A. M. van der Zande, P. Huang, S. Jockusch, J. Hone, D. R. Reichman, L. E. Brus, T. F. Heinz, Energy transfer from quantum dots to graphene and MoS_2: The role of absorption and screening in two-dimensional materials. *Nano Lett.* **16**, 2328–2333 (2016).
47. K. Wu, J. Chen, J. R. McBride, T. Lian, Efficient hot-electron transfer by a plasmon-induced interfacial charge-transfer transition. *Science* **349**, 632–635 (2015).
48. Y. Liang, S. Huang, R. Soklaski, L. Yang, Quasiparticle band-edge energy and band offsets of monolayer of molybdenum and tungsten chalcogenides. *Appl. Phys. Lett.* **103**, 042106 (2013).
49. A. Chernikov, C. Ruppert, H. M. Hill, A. F. Rigosi, T. F. Heinz, Population inversion and giant bandgap renormalization in atomically thin WS_2 layers. *Nat. Photonics* **9**, 466–470 (2015).
50. E. J. Sie, A. Steinhoff, C. Gies, C. H. Lui, Q. Ma, M. Rösner, G. Schönhoff, F. Jahnke, T. O. Wehling, Y.-H. Lee, J. Kong, P. Jarillo-Herrero, N. Gedik, Observation of exciton redshift–blueshift crossover in monolayer WS_2. *Nano Lett.* **17**, 4210–4216 (2017).
51. M. M. Ugeda, A. J. Bradley, S.-F. Shi, F. H. da Jornada, Y. Zhang, D. Y. Qiu, W. Ruan, S.-K. Mo, Z. Hussain, Z.-X. Shen, F. Wang, S. G. Louie, M. F. Crommie, Giant bandgap renormalization and excitonic effects in a monolayer transition metal dichalcogenide semiconductor. *Nat. Mater.* **13**, 1091–1095 (2014).
52. A. Raja, A. Chaves, J. Yu, G. Arefe, H. M. Hill, A. F. Rigosi, T. C. Berkelbach, P. Nagler, C. Schüller, T. Korn, C. Nuckolls, J. Hone, L. E. Brus, T. F. Heinz, D. R. Reichman, A. Chernikov, Coulomb engineering of the bandgap and excitons in two-dimensional materials. *Nat. Commun.* **8**, 15251 (2017).
53. J. Miyazaki, K. Kawasumi, T. Kobayashi, Resolution improvement in laser diode-based pump–probe microscopy with an annular pupil filter. *Opt. Lett.* **39**, 4219–4222 (2014).
54. K. J. Tielrooij, L. Piatkowski, M. Massicotte, A. Woessner, Q. Ma, Y. Lee, K. S. Myhro, C. N. Lau, P. Jarillo-Herrero, N. F. van Hulst, F. H. L. Koppens, Generation of photovoltage in graphene on a femtosecond timescale through efficient carrier heating. *Nat. Nanotechnol.* **10**, 437–443 (2015).
55. L. Yuan, L. Huang, Exciton dynamics and annihilation in WS_2 2D semiconductors. *Nanoscale* **7**, 7402–7408 (2015).
56. T. F. Chung, T. Shen, H. Cao, L. A. Jauregui, W. Wu, Q. Yu, D. Newell, Y. P. Chen, Synthetic graphene grown by chemical vapor deposition on copper foils. *Int. J. Mod. Phys. B* **27**, 1341002 (2013).
57. N. Petrone, C. R. Dean, I. Meric, A. M. van der Zande, P. Y. Huang, L. Wang, D. Muller, K. L. Shepard, J. Hone, Chemical vapor deposition-derived graphene with electrical performance of exfoliated graphene. *Nano Lett.* **12**, 2751–2756 (2012).
58. G. Bian, T.-F. Chung, C. Chen, C. Liu, T.-R. Chang, T. Wu, I. Belopolski, H. Zheng, S.-Y. Xu, D. S. Sanchez, N. Alidoust, J. Pierce, B. Quilliams, P. P. Barletta, S. Lorcy, J. Avila, G. Chang, H. Lin, H.-T. Jeng, M.-C. Asensio, Y. P. Chen, M. Z. Hasan, Experimental observation of two massless Dirac-fermion gases in graphene-topological insulator heterostructure. *2D Mater.* **3**, 021009 (2016).
59. K. F. Mak, J. Shan, T. F. Heinz, Seeing many-body effects in single- and few-layer graphene: Observation of two-dimensional saddle-point excitons. *Phys. Rev. Lett.* **106**, 046401 (2011).
60. R. Dovesi, *CRYSTAL09 User's Manual and Documentation* (University of Turin, 2009).
61. M. Catti, A. Pavese, R. Dovesi, V. R. Saunders, Static lattice and electron properties of $MgCO_3$ (magnesite) calculated by ab initio periodic Hartree-Fock methods. *Phys. Rev. B Condens. Matter* **47**, 9189–9198 (1993).

62. A. Lichanot, E. Aprà, R. Dovesi, Quantum mechnical Hartree-Fock study of the elastic properties of Li_2S and Na_2S. *Phys. Status Solidi B Basic Solid State Phys.* **177**, 157–163 (1993).
63. F. Corà, A. Patel, N. M. Harrison, R. Dovesi, C. R. A. Catlow, An ab initio Hartree–Fock study of the cubic and tetragonal phases of bulk tungsten trioxide. *J. Am. Chem. Soc.* **118**, 12174–12182 (1996).
64. J. P. Perdew, K. Burke, M. Ernzerhof, Generalized gradient approximation made simple. *Phys. Rev. Lett.* **77**, 3865–3868 (1996).
65. S. Grimme, Semiempirical GGA-type density functional constructed with a long-range dispersion correction. *J. Comput. Chem.* **27**, 1787–1799 (2006).
66. G. Kresse, J. Furthmüller, Efficient iterative schemes for ab initio total-energy calculations using a plane-wave basis set. *Phys. Rev. B Condens. Matter* **54**, 11169–11186 (1996).
67. P. E. Blöchl, Projector augmented-wave method. *Phys. Rev. B Condens. Matter* **50**, 17953–17979 (1994).
68. G. Kresse, D. Joubert, From ultrasoft pseudopotentials to the projector augmented-wave method. *Phys. Rev. B Condens. Matter* **59**, 1758–1775 (1999).
69. J. Heyd, G. E. Scuseria, M. Ernzerhof, Hybrid functionals based on a screened Coulomb potential. *J. Chem. Phys.* **118**, 8207–8215 (2003).
70. S. Chong, W. Min, X. S. Xie, Ground-state depletion microscopy: Detection sensitivity of single-molecule optical absorption at room temperature. *J. Phys. Chem. Lett.* **1**, 3316–3322 (2010).
71. C. T. O. Wong, S. S. Lo, L. Huang, Ultrafast spatial imaging of charge dynamics in heterogeneous polymer blends. *J. Phys. Chem. Lett.* **3**, 879–884 (2012).
72. J. E. Lee, G. Ahn, J. Shim, Y. S. Lee, S. Ryu, Optical separation of mechanical strain from charge doping in graphene. *Nat. Commun.* **3**, 1024 (2012).
73. J. Yan, Y. Zhang, P. Kim, A. Pinczuk, Electric field effect tuning of electron-phonon coupling in graphene. *Phys. Rev. Lett.* **98**, 166802 (2007).

Acknowledgments: A.K. thanks Y. Ma for his help on VASP and A. Chernikov for discussions. L.Y. thanks W. Hu for discussions. **Funding:** L.H. and L.Y. acknowledge the support from the NSF under award number 1433490 and from U.S. Department of Energy, Office of Basic Energy Sciences through award DE-SC0016356. Y.P.C. and T.-F.C. acknowledge the support from the NSF Civil, Mechanical and Manufacturing Innovation program (CMMI 1538360) as well as the EFMA program through grant no. 1641101. T.-F.C. also acknowledges support from the Purdue University Bilsland Dissertation Fellowship. A.K. and T.H. acknowledge ZIH Dresden for computational support and Deutsche Forschungsgemeinschaft (DFG) for grants HE 3543/27-1 and GRK 2247/1 (QM3). **Author contributions:** L.H. and Y.P.C. designed the experiments. L.Y. and T.-F.C. carried out the measurements. Y.W. and Y.X. contributed to instrument development and sample preparation. L.Y., T.-F.C., and L.H. analyzed experimental data. A.K. and T.H. carried out and analyzed the DFT calculations. L.Y. and L.H. wrote the manuscript. All authors contributed to editing of the manuscript. **Competing interests:** The authors declare that they have no competing interests. **Data and materials availability:** All data needed to evaluate the conclusions in the paper are present in the paper and/or the Supplementary Materials. Additional data related to this paper may be requested from the authors.

Submitted 31 January 2017
Accepted 2 January 2018
Published 2 February 2018
10.1126/sciadv.1700324

Citation: L. Yuan, T.-F. Chung, A. Kuc, Y. Wan, Y. Xu, Y. P. Chen, T. Heine, L. Huang, Photocarrier generation from interlayer charge-transfer transitions in WS_2-graphene heterostructures. *Sci. Adv.* **4**, e1700324 (2018).

Science Advances

Photocarrier generation from interlayer charge-transfer transitions in WS_2-graphene heterostructures

Long Yuan, Ting-Fung Chung, Agnieszka Kuc, Yan Wan, Yang Xu, Yong P. Chen, Thomas Heine and Libai Huang

Sci Adv **4** (2), e1700324.
DOI: 10.1126/sciadv.1700324